

Journal of Materials Chemistry C

Accepted Manuscript



This is an *Accepted Manuscript*, which has been through the Royal Society of Chemistry peer review process and has been accepted for publication.

Accepted Manuscripts are published online shortly after acceptance, before technical editing, formatting and proof reading. Using this free service, authors can make their results available to the community, in citable form, before we publish the edited article. We will replace this *Accepted Manuscript* with the edited and formatted *Advance Article* as soon as it is available.

You can find more information about *Accepted Manuscripts* in the [Information for Authors](#).

Please note that technical editing may introduce minor changes to the text and/or graphics, which may alter content. The journal's standard [Terms & Conditions](#) and the [Ethical guidelines](#) still apply. In no event shall the Royal Society of Chemistry be held responsible for any errors or omissions in this *Accepted Manuscript* or any consequences arising from the use of any information it contains.

Review

Electrical Characterization of Nanocrystal Solids

Cite this: DOI: 10.1039/x0xx00000x

D. Bozyigit,^a and V. Wood^b

Received 00th January 2012,

Accepted 00th January 2012

DOI: 10.1039/x0xx00000x

www.rsc.org/

Here we provide a primer for correctly selecting and implementing optoelectronic characterization techniques on semiconductor nanocrystal solids and choosing the appropriate models with which to interpret the data. We discuss the two most fundamental device architectures incorporating a solid composed of solution-processed semiconductor nanocrystals: the metal-semiconductor-metal diode and the heterojunction diode, and the broad classes of techniques that can be used to analyse them including quasi-static (e.g. current-voltage), harmonic (e.g. admittance spectroscopy), and transient measurements. We then separately address the models that are commonly applied to understand the semiconductor behaviour including the Shockley diode equation and capacitance-based analyses such as Mott-Schottky and Shockley-Read-Hall models and potential pitfalls in their application. We additionally highlight methods to extract the density and position of trap states, located in the band gap of these semiconductors and which play an important role in device performance. Due to its interest as an absorptive material for third generation solar cells, we discuss the techniques and analysis in the context of PbS nanocrystal solids and provide reference values for this material throughout the text.

Table of Contents:

I. Introduction

II. Devices and Measurement Setup

- A. Device Architectures
- B. Measurement Setup

III. Optoelectronic Measurement Techniques

- A. Quasi-static Techniques
- B. Harmonic Techniques
- C. Transient Techniques

IV. Interpretation of Data

- A. Shockley Diode Equation
- B. Capacitance Models
- C. Mott-Schottky Model
- D. Shockley-Read-Hall Model
- E. Trap State Characterization

V. Conclusions

I. Introduction

The impressive advances in colloidal chemistry in the past twenty years have enabled the advent of solution-processed semiconductors assembled from preformed nanocrystals (NCs).¹ These semiconductors not only offer the possibility for low cost manufacturing and processing on flexible substrates, but also enable the integration of quantum-confined materials with their unique electronic and optical properties into large-area devices. These features make nanocrystal-based solids particularly attractive for optoelectronic applications, such as LEDs², photodetectors,³ and solar cells.⁴⁻⁷

However, NC-based semiconductors present challenges for electric characterization. The disordered nature of the nanocrystal solid, the large surface area of the nanocrystals, and their hybrid nature with inorganic cores and organic ligands, introduce large numbers of electronic trap states, a broad window of characteristic times scales for charge carrier dynamics, and often a mix of localized and band-like transport.⁸ Nonetheless, many of the characterization techniques and models developed over the past fifty years to understand transport in crystalline and polycrystalline materials can be applied to understanding the electronic properties of nanocrystal solids. This must be done carefully, with a clear understanding of the limitations of the measurement techniques and the assumptions behind the models.

Here we aim to provide a compact description of optoelectronic measurement techniques and common pitfalls facing their application to nanocrystal solids. In particular, we emphasize the importance of distinguishing between the physical measurement and the application of models to interpret the measurement results.

II. Devices and Measurement Techniques

Device Architectures

While a variety of different architectures have been conceived for nanocrystal-based solar cells,⁶ here we focus on the two most fundamental: the metal-semiconductor-metal (MSM) diode and the heterojunction (HJ) diode.

The simplest device to characterize the photovoltaic and electronic properties of a semiconductor is the metal-semiconductor-metal (MSM) diode. As depicted in Figure 1a, in this device architecture, a metal with high workfunction (ϕ_p) is used to extract holes while a metal with a low workfunction (ϕ_n) is used to extract electrons. Like all solar cells, the MSM diode derives its photovoltaic effect from the carrier-type selectivity of these contacts.⁹ This selectivity is primarily

provided by the built-in field, which stems from the difference in workfunction between the two contacts: $\phi_p - \phi_n$.

Due to the presence of the metal-semiconductor interfaces, NC-based MSM diodes are often referred to as “Schottky-diodes” in reference to the applicability of the Schottky-model to crystalline semiconductor-based MSM-diodes.^{10,11} However, it is unclear if the charge transport physics in the NC-based MSM-diode is related to the majority-carrier Schottky-model.

NC-based MSM-diodes are advantageous over record-performing NC-based devices for characterizing the physical properties of a NC-solid due to their ease of fabrication and the fact that they only contain one semiconducting material.^{11–16} However, a disadvantage is that the low-workfunction metals that are used as electrodes, such as Al, Mg, Ca, are easily oxidized and hydrolyzed,¹⁷ and the metal-semiconductor interface is sensitive to this degradation.

It has been shown that the properties of the metal electrodes can be improved by introducing thin metal-oxide or salt layers. For the hole-extracting electrode, transition metal oxide layers, such as MoO₃ and VaO_x, ~10 nm in thickness, have improved

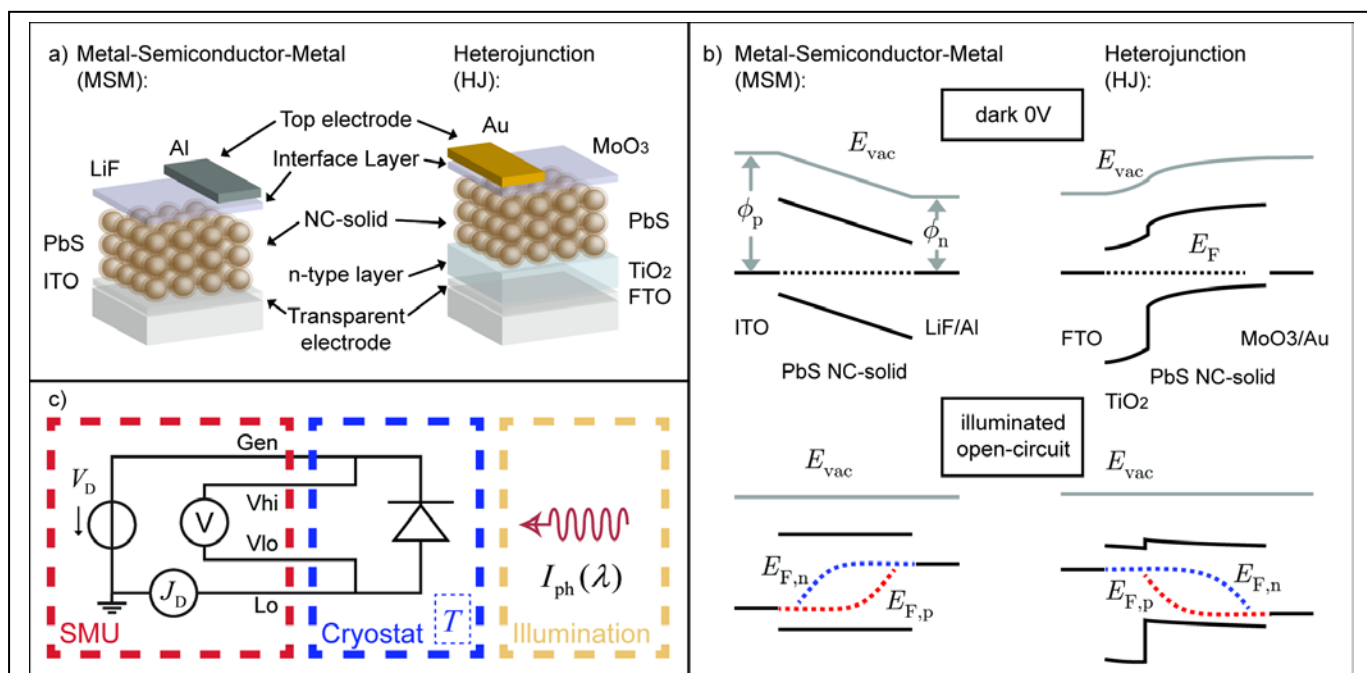


Figure 1: a) Schematics of the two fundamental device architectures for NC solar cells: the MSM-diode and the HJ-diode. Common materials for each layer are indicated. b) Band alignment under open circuit conditions for MSM-diode (left) and the HJ-diode (right) in the dark (top) and under illumination (bottom). In the dark, parts of the diode are depleted and an electric field is present, as indicated by the slope of the vacuum energy E_{vac} . Under illumination, the quasi-Fermi energies for electrons and holes split and establish a chemical potential, which is the source of the open-circuit voltage. No electric field is present at open-circuit condition, as the free charge carriers screen the electric field. c) Schematic of a generic optoelectronic characterization system. The source-measure-unit (SMU) applies a voltage to the diode (V_D) and measures the current (J_D). The diode is in a cryostat that controls the temperature (T) and the atmosphere. Depending on the type of measurement, illumination ($I_{ph}(\lambda)$) is provided by a broad-band or monochromatic light source.

performance.^{18–20} On the electron-extracting electrode, LiF (~1.0nm) is used to improve the open-circuit voltage and the stability under ambient conditions.^{15,17} In the bulk, MoO₃ and LiF are wide band gap insulators and would be expected to impede charge transport. As thin layers, it is suspected that they pin the Fermi-energy at the semiconductor-metal interface at an advantageous position that increases the carrier selectivity of the electrode, while allowing charge extraction through trap state mediated transport.^{17–19} Additionally, the metal-oxide interlayers can act as charge carrier blocking layers and physical buffer layers, further enhancing solar cell performance.¹⁸ An excellent review on this topic was recently published by Greiner and Lu.²¹

The current record power conversion efficiency for a MSM solar cell with a PbS NC-solid is 5.2% and 4.6% for a PbSe NC-solid.^{22,16} The efficiency of this architecture is limited by short charge carrier diffusion lengths, which restrict the maximum film thickness to 100 – 200nm.⁵ Although some reports claim that the MSM-diode has intrinsically low open-circuit voltages and fill factors, there exist several reports with open-circuit voltages and fill factors on par with record performing devices.^{23–25}

As shown in Figure 1a, the heterojunction (HJ) diode consists of an n-type semiconductor and a p-type semiconductor, which are ohmically contacted to a low-workfunction and a high-workfunction metal respectively. The advantage of the HJ over the MSM is the improved spatial separation of charge carriers, which reduces recombination losses. This comes at the cost of increased complexity in device fabrication and characterization.

In a typical HJ diode, an n-type metal oxide (TiO₂ or ZnO) is used to extract electrons, and the NC-solid is used as a p-type layer to extract hole carriers. Light absorption takes place predominantly in the PbS NC-solid. Variations to the HJ structure have been reported, including planar HJs^{18,19,26–30} and nano-structured bulk-heterojunctions (BHJs).^{31–36} The currently certified maximum power conversion efficiency of such devices is at 7.0%.³⁰ In a second variety of HJs, the n-type layer is provided by an n-type NC-solid. Again, planar^{37,38} and BHJ^{39,40} geometries have been reported. Currently, 4.9% is the highest reported power conversion efficiency in this category.⁴⁰

Measurement Setup

As shown in Figure 1c, for complete physical characterization of a device, a measurement setup must offer: reliable electrical contacts, optical access, accurate temperature control and measurement, and environmental control.

Environmental control is desirable as NC-based semiconductors are highly sensitive to atmospheric oxygen and water

vapour.^{11,17,41,25} Temperature dependent measurements on diodes are used to determine various activation energies in the system. This requires that the electrical contacting mechanism be robust to temperature change.

Regardless of the means for electrical contact, a source-measure-unit (SMU) is needed. This device (or a collection of devices) has four terminals. The *Generator* terminal is connected to a voltage source, which supplies a voltage (V_D) to the device. The second terminal (*Lo*) is connected to a device that measures the current coming back from the diode. In this review, we consistently refer to the current density (J_D), where the current is normalized by the characteristic device area to facilitate comparison between different device geometries. The remaining two terminals (*Vhi*, *Vlo*) are connected to a high impedance ($\gg 1\text{M}\Omega$) voltage measurement device to measure V_D .

III. Optoelectronic Characterization Techniques

In this section, we describe optoelectronic measurement techniques that are most relevant for NC-based solar cells and the specifics (e.g. instrumentation) of how these measurements are implemented. For a more complete overview, we recommend *Electrical Characterization of Organic Electronic Materials and Devices*⁴² by Peter Stallinga or *Advanced Characterization Techniques for Thin Film Solar Cells* by Abou-Ras, Kirshartz and Rau.⁴³

To facilitate discussion, we classify the techniques in three different groups that depend on their temporal requirements for the SMU: (1) quasi-static, (2) harmonic, and (3) transient.

To extract physical parameters from these measurements, the data has to be interpreted in the context of specific models of the device physics, which we describe separately in Section IV. This is done to emphasize the importance of reporting the raw data from these characterization techniques prior to analysis of the data through application of a specific model, which is often borrowed from classical or organic electronics and has not to date been validated for nanocrystal-based devices.

Quasi-static Techniques

The most common and straightforward optoelectronic characterization techniques are quasi-static measurements, in which a constant V_D is applied and J_D is measured, yielding a current-voltage (IV) curve. These measurements can be performed with a SMU such as the Keithley 2400. Representative data for a MSM diode with a benzenedithiol (BDT)-treated PbS NC-based semiconductor layer are provided in the inset in Figure (2a).^{23,44}

Measuring the IV curve under illumination with a standardized solar spectrum is used to determine the performance parameters of the solar cell: the open-circuit voltage (V_{oc}), the short-circuit current-density, (J_{sc}), and the power conversion efficiency (η). Due to the interest in assessing the uniformity of the solution-processed semiconductor layer in the different devices on the same substrate or across several different substrates, it is helpful to report uncertainties obtained from a statistically relevant number of devices. Measurement of V_{oc} and J_{sc} for different illumination intensities (Figure 2b), and temperatures (Figure 2c) are performed to obtain information on the charge transport in the diode.^{23,44} In Section IV, we discuss the physical parameters that can be obtained from such measurements by application of the Shockley diode equation.

Harmonic Techniques

The second class of optoelectronic characterization involves application of a frequency dependent voltage or illumination and measurement of the system response.

Admittance Spectroscopy

When the diode is biased at a certain level $V_{D,0}$ with an additional harmonic signal of frequency $f = \omega / 2\pi$, such that $V_D(\omega) = V_{D,0} + \delta\hat{V}_D \sin \omega$, the response to this excitation is measured as

$$J_D(\omega) = J_{D,0} + \delta\hat{J}_X \sin \omega + \delta\hat{J}_Y \cos \omega \quad (1.1)$$

where $\delta\hat{J}_X$ and $\delta\hat{J}_Y$ are the in-phase and out-of-phase components of the current.

In most cases, an impedance analyzer is used to perform such measurements. However, an impedance analyser simply consists of a harmonic voltage source and a lock-in amplifier, and harmonic measurements can also be carried out using an arbitrary waveform generator (AWG) in combination with a lock-in amplifier to measure the in-phase and out-of-phase components.

From these values the complex admittance can be calculated:

$$Y(\omega) = Y'(\omega) + iY''(\omega) = \delta\hat{J}_X / \delta\hat{V}_D + i\delta\hat{J}_Y / \delta\hat{V}_D$$

where Y' and Y'' are the real and imaginary parts of the admittance and i is the imaginary number. The admittance can be transformed into other equivalent representations,⁴⁵ such as the complex capacitance, which is often the most useful in the context of semiconductor diodes:

$$C(\omega) = C'(\omega) + iC''(\omega) = \frac{iY(\omega)}{\omega}, \quad (1.2)$$

where C' is the real part and C'' the imaginary part of the capacitance. In well behaved systems, C' and C'' are coupled by the Kramers-Kronig relations, which means that C' and

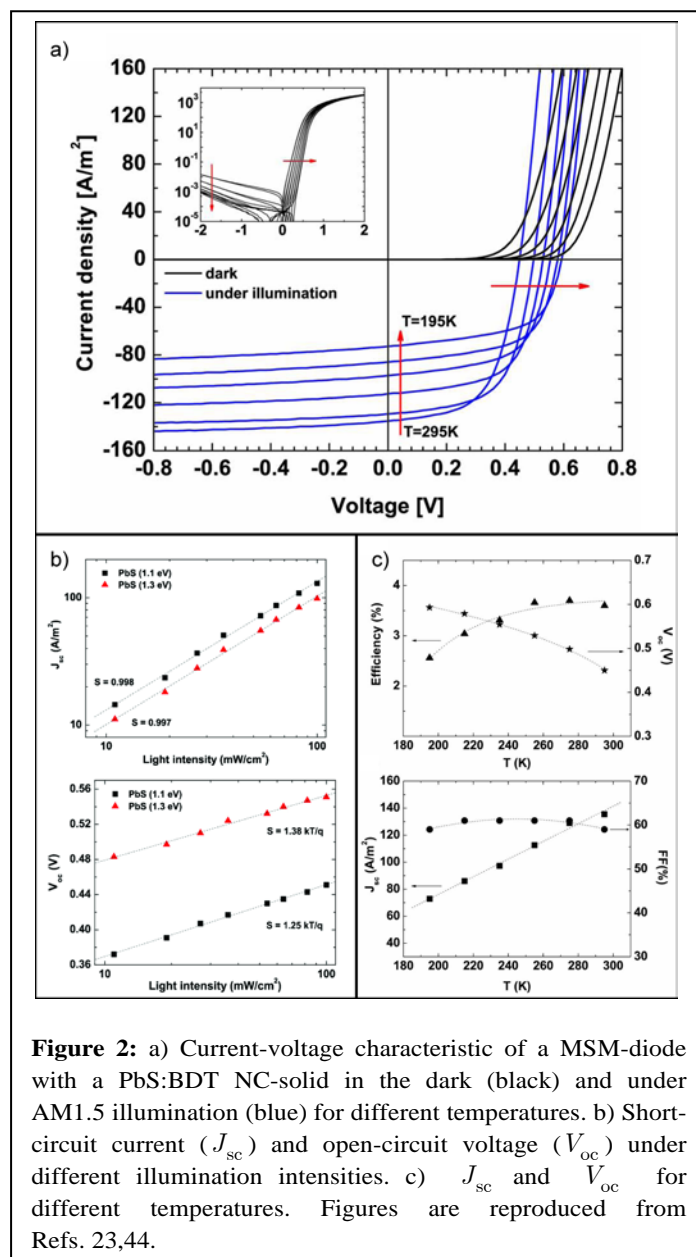


Figure 2: a) Current-voltage characteristic of a MSM-diode with a PbS:BDT NC-solid in the dark (black) and under AM1.5 illumination (blue) for different temperatures. b) Short-circuit current (J_{sc}) and open-circuit voltage (V_{oc}) under different illumination intensities. c) J_{sc} and V_{oc} for different temperatures. Figures are reproduced from Refs. 23,44.

C'' contain essentially the same information.⁴⁵ It is therefore sufficient for most practical purposes of diode characterization to only investigate C' .

Some authors discuss capacitance measurements in terms of the absolute value of the capacitance, given by $|C| = \sqrt{C'^2 + C''^2}$. While this is not incorrect per se, one must keep in mind that physical models, such as the Mott-Schottky model, which are developed for C' , cannot be applied to $|C|$ (See Section IV).

Figures 3a and 3b provide examples of common types of capacitive measurements that have been performed on PbS NC-solids. Capacitance versus frequency measurements at different temperatures (Figure 3a), also known as thermal admittance spectroscopy (TAS), can be used to obtain information on trap

states using the Shockley-Read-Hall trapping model.^{25,30} Capacitance versus voltage measurements, as shown in Figure 3b, and are used to determine the built-in voltage of the diode and the doping density of the semiconductor using the Mott-Schottky model of the depletion region.¹⁰

Photocurrent Spectroscopy

A second group of harmonic techniques is known as photocurrent spectroscopy. Here, the illumination is modulated $I_D(\omega) = I_{D,0} + \delta \hat{I}_D \sin \omega$ using a chopper and the current response is recorded using a lock-in amplifier. The diode is usually reverse biased ($V_D \leq 0V$) to facilitate extraction of photo-excited charge carriers. In contrast to admittance measurements, the photocurrent is most practically discussed in terms of its magnitude ($|J_{D,ph}(\omega)|$) and phase ($\varphi_{D,ph}(\omega)$):

$$\begin{aligned} |J_{D,ph}(\omega)| &= \sqrt{\delta \hat{J}_x^2 + \delta \hat{J}_y^2}, \\ \varphi_{D,ph}(\omega) &= \arctan \frac{\delta \hat{J}_x}{\delta \hat{J}_y} \end{aligned} \quad (1.3)$$

The most common variation of photocurrent spectroscopy is the measurement to determine the external quantum efficiency (EQE) of a device, as shown in Figure 3c.⁴¹ Here, a fixed chopping frequency in the range of 10 – 1000Hz is set and the wavelength λ of a monochromatic light source is tuned from the UV to the NIR while the photocurrent is recorded. To obtain the EQE, the same measurement is performed on a calibrated reference device with a known EQE.

This technique can be extended to the mid and far-infrared region using a Fourier transform infrared spectrometer (FTIR), which is known as Fourier transform infrared photocurrent spectroscopy (FTPS)⁴⁶. This technique was recently applied to PbS NC-diodes and revealed a discrete optical transition within the bandgap indicative of a trap state (See Figure 3d).²⁵

Alternatively, changing frequency of the light modulation is known as intensity-modulated photocurrent spectroscopy (IMPS),^{47,48} which was recently applied by Erslev et al. to investigate the Urbach tail in PbS NC solids (See Figure 3e).⁴⁹

Transient Techniques

In the third class of optoelectronic characterization techniques, an electrical or optical pulse form is applied to the device, and the voltage or current response is recorded as a function of time.

Most commonly, a voltage signal, $V_D(t)$, with the form of a ramp or pulse, is applied to the diode using an AWG. The time dependent current $J_D(t)$ is measured, typically by a combination of a broad-band transimpedance amplifier and a

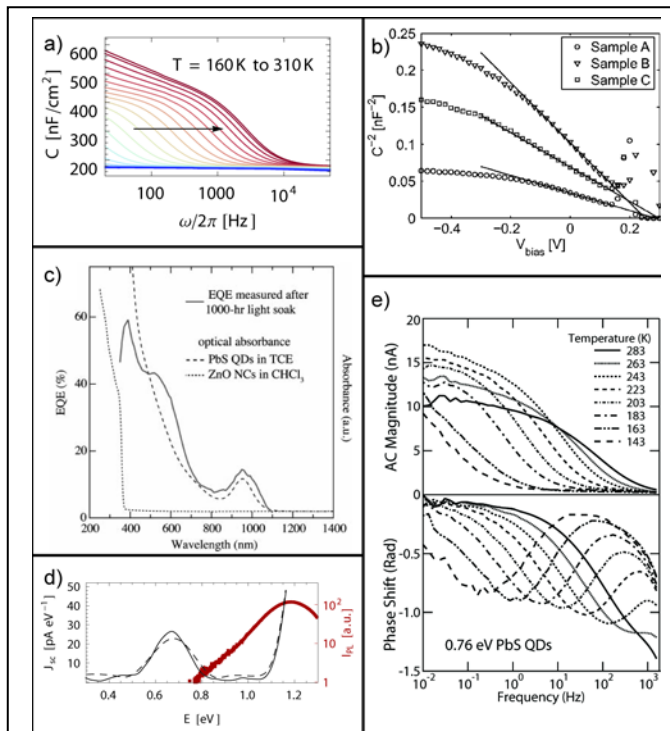


Figure 3: Different harmonic measurement techniques applied to PbS NC-solid diodes. a) Capacitance vs. frequency at 0 V bias for different temperatures (thermal admittance spectroscopy (TAS)).²⁵ b) Capacitance vs. voltage at 20 Hz (Mott-Schottky analysis).¹⁰ c) External quantum efficiency (EQE) for illumination wavelengths.⁴¹ d) Photocurrent vs. illumination for near to far-infrared illumination (FTPS).²⁵ e) Photocurrent for different modulation frequencies (IMPS).⁴⁹ Figures are reproduced from the indicated references.

digitizer, or with the low-impedance input of an oscilloscope, if the sensitivity of the latter is sufficient.

Example $V_D(t)$ profiles and $J_D(t)$ measurement traces are shown in Figure 4.^{50,51} The linear voltage ramp in Figure 4a is a Charge Extraction by Linearly Increasing Voltage (CELIV) measurement. CELIV was designed to determine charge carrier mobilities in organic semiconductors,^{52,53} and has been applied to PbS NC-solids to determine the majority carrier mobility⁵⁴ and the dielectric constant.^{50,10} The rectangular pulse in Figure 4b is for charge (Q)-based Deep Level Transient Spectroscopy (Q-DLTS) measurements, which can be used to determine trap activation energies and trap densities based on the Shockley-Read-Hall (SRH) model.

In photovoltage transient techniques, the sample is illuminated by a constant light source superimposed with a short laser pulse, such that the measured $V_{oc}(t)$ shows a small transient (Figure 3c, left). Such transient open-circuit voltage measurements rely on the use of a high impedance voltage measurement device. A regular oscilloscope input with $R_{in} = 1M\Omega$ can be too low and will limit the longest

recombination time that can be measured to $R_{in}C \approx 1\text{ms}$, where C is the high frequency capacitance of the diode. Instead, broadband voltage amplifiers with up to $1\text{T}\Omega$ input impedance are preferable.

Photovoltage transient measurements are often accompanied by measurement of the photocurrent transient, $J_{sc}(t)$. This is done with a broadband transimpedance amplifier and is used to determine the amount of charge introduced by the light pulse and the charge extraction time.⁵⁵ A typical photocurrent transient is shown in Figure 3c (right).³⁰

IV. Interpretation of Data

To interpret the quasistatic, harmonic, and transient measurements described above, various models are applied. Here we discuss the key models for extracting parameters of relevance to solar cell performance, the underlying physical assumptions of these models, and the considerations that must be taken in applying them to NC-based solids.

The Shockley Diode Equation

The most fundamental characteristic of a diode is its IV curve, which is generally analysed using the Shockley Diode equation. Here we use the notation in the review by Lunt *et al.*:⁵

$$J_D = \frac{R_p}{(1.4)R_s + R_p} \left\{ J_0 \left[\exp\left(\frac{e(V_D - J_D R_s)}{n_V kT}\right) - 1 \right] \right\} + \frac{V_D}{R_p} - J_{sc},$$

where R_p is the shunt resistance, R_s the series resistance, V_D the voltage across the device, J_{sc} the short circuit current, n_V the ideality factor related to the voltage, k the Boltzmann constant, and J_0 the reverse saturation current. The Shockley diode equation is phenomenological so its parameters are not unambiguously linked to specific physical processes.

The low-forward bias region between 0.1 to 1V, where the current increases exponentially, is the most important for solar cell performance. The exponential current increase in the dark is described by the reverse saturation current (J_0) and the ideality factor related to voltage (n_V). Typical values of J_0 for PbS nanocrystal diodes at room temperature range from $10^{-4} - 10^{-7} \text{ mA/cm}^2$.^{10,44,24} J_0 derives its name from the fact that ideal diodes saturate to this current in the reverse region. In the context of solution processed semiconductor based devices, the name *reverse saturation current* is rather misleading, as this current is hardly ever observed due to the presence of larger leakage currents that dominate in reverse bias.

In all common physical diode models, J_0 is associated with a thermal activation energy E_{JA} and is given by:

$$J_0 = J_{00} \exp\left(\frac{-E_{JA}}{n_E kT}\right), \quad (1.5)$$

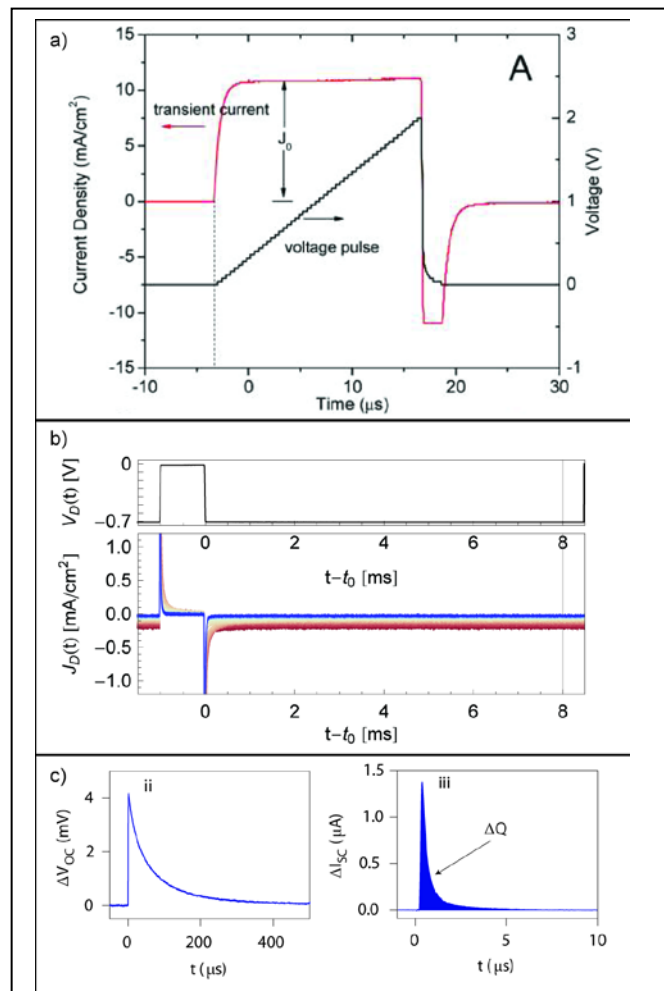


Figure 4: Transient measurement techniques. a) Voltage ramp is applied and transient current is measured (CELIV).⁵⁰ b) Voltage pulse is applied and transient current is measured (Q-DLTS).⁵¹ c) Small laser pulse is applied and small transient distortion in the open-circuit voltage is measured (left). In a second measurement the short-circuit current of the same laser pulse is measured (right) to obtain the differential charge Δq .³⁰ Figures are reproduced from the indicated references.

where n_E is the ideality factor related to the activation energy. We distinguish between the ideality factors n_V and n_E to facilitate the discussion of existing literature below.

For a semiconductor with a band gap E_g , E_{JA} , and n_E assume different values depending on the dominant mode of charge conduction. In the case of:

- Band-to-band recombination in an ideal diode, $E_{JA} = E_g$ and $n_E = n_V = 1$
- Trap-assisted band-to-band recombination, $E_{JA} = E_g$ and $n_E = n_V = 2$
- Ideal thermoionic-emission or diffusion of majority carriers over a Schottky-barrier with height ϕ_B , $E_{JA} = \phi_B$ and $n_E = n_V = 1$

A mixture of direct band-to-band recombination ($n_E = n_V = 1$) and trap-assisted band-to-band recombination ($n_E = n_V = 2$) can lead to ideality factors in the range of 1 to 2.^{56,57} While it was proposed that space charge effects can increase the ideality factor in organic semiconductors,⁵⁸ in light of the high dielectric constant of PbS NC-solids, we expect that space charge limited conduction is improbable and that trap assisted recombination would be the source of increased ideality factors, in agreement with the findings in Ref. 23.

Equation (1.5) shows that any assumption made about n_E , directly affects the determination of the activation energy, E_{JA} . This has resulted in a range of different values of E_{JA} reported in literature. Using three distinct data sets - temperature dependent IV characteristics, temperature-dependent open circuit voltage measurements, and optical absorption - reported by Szendrei et al.⁴⁴ - we show how the relevant parameters n_V , J_{00} , and E_{JA} can be determined self-consistently.

First, we take the model used for thin-film photovoltaics, where $n_E = n_V$.⁵⁹ Now, the open-circuit voltage can be calculated from Eq. (1.4) and (1.5) to be:

$$V_{oc} = E_{JA} + \frac{n_V kT}{e} \log \left(\frac{J_{sc}}{J_{00}} \right). \quad (1.6)$$

We fit Eq. (1.6) to the IV characteristics in the dark at room temperature and determine $n_V = 1.6$ (Figure 5a). Setting $n_E = n_V = 1.6$, we then fit Eq. (1.5) to J_0 determined at different temperatures and find $E_{JA} = 0.91$ eV and $J_{00} = 1.7 \times 10^5$ mA/cm². Alternatively, in Figure 5c, we plot the temperature-dependent open-circuit voltage data with a fit of Eq. (1.6) and find $E_{JA} = 0.92$ eV. Finally, we fit the optical absorption tail of the NCs according to a direct semiconductor model and obtain a band gap of $E_g = 0.93$ eV. The agreement of the energies determined using three separate data sets convinces us that $n_E = n_V$ is a valid assumption for NC-solids.

Furthermore, the strong agreement between the extracted parameters demonstrates the importance of distinguishing between the optical absorption exciton energy (E_{exc}) and the charge transport bandgap. As explained above, we find from the data in Ref. 44 that $E_{JA} = E_g = 0.92$ eV is the effective bandgap for charge transport while $E_{exc} = 1.1$ eV. A recent report shows that J_0 scales with the exciton energy according to $E_{JA} = E_{exc}$ with $n_E = 1.92$ and $n_V = 1.7 - 2.4$.²⁴ However, if the 15% discrepancy between E_g and E_{exc} is accounted for, an ideality factor of $n_E = 1.6$ is obtained for the data in Ref. 24. Thus the data in Ref. 24 and Ref. 44 are actually in very good agreement.

For the case of ITO/PbS/LiF/Al MSM diodes, we thus conclude that the:

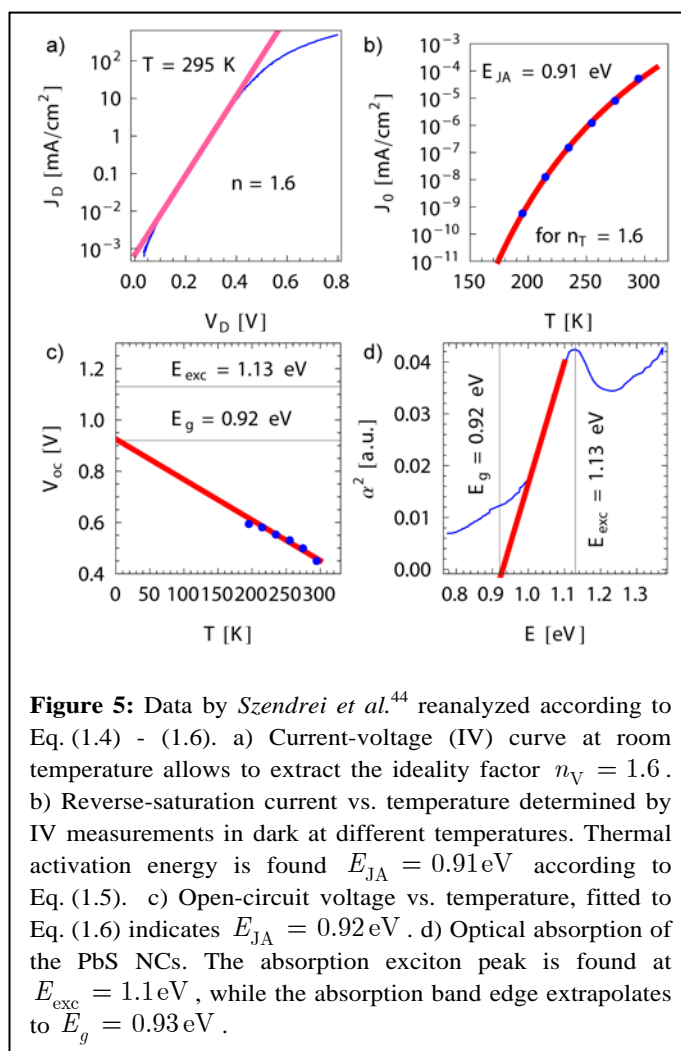


Figure 5: Data by Szendrei et al.⁴⁴ reanalyzed according to Eq. (1.4) - (1.6). a) Current-voltage (IV) curve at room temperature allows to extract the ideality factor $n_V = 1.6$. b) Reverse-saturation current vs. temperature determined by IV measurements in dark at different temperatures. Thermal activation energy is found $E_{JA} = 0.91$ eV according to Eq. (1.5). c) Open-circuit voltage vs. temperature, fitted to Eq. (1.6) indicates $E_{JA} = 0.92$ eV. d) Optical absorption of the PbS NCs. The absorption exciton peak is found at $E_{exc} = 1.1$ eV, while the absorption band edge extrapolates to $E_g = 0.93$ eV.

- forward current has an activation energy, which is the effective bandgap for charge transport $E_{JA} = E_g$, which can be $\sim 15\%$ smaller than the absorption-exciton energy (E_{exc}).
- ideality factors ($n_E = n_V$) are in the range of 1.6 - 2.0, indicating a mixture of direct recombination and trap-assisted recombination.

Capacitance Models

The performance of a semiconductor can be highly influenced by the presence of states within the band gap such as dopants or trap states. These states are fundamentally related to the capacitance of the semiconductor, and most models that are used to determine the number, density, and properties of midgap states are therefore based on different measurements of the capacitance.

A semiconductor diode has two major capacitance contributions: the electrostatic capacitance of the depletion region (C_D) and the chemical capacitance (C_T) of the electronic states of the semiconductor material, as shown in Figure 6a.

The electrostatic capacitance can be understood as a plate capacitor over the depletion region, where no or few free charge carriers are present, and is given by

$$C_D = \frac{\epsilon_s \epsilon_0}{W_D}, \quad (1.7)$$

where ϵ_s is the dielectric constant of the semiconductor and W_D is the width of the depletion region. The dielectric constant of a NC-solid can be calculated by the Maxwell-Garnett effective medium theory if the volume filling fraction (δ) of NCs is known:

$$\epsilon_s = \epsilon_h \frac{\epsilon_{nc}(1 + 2\delta) - \epsilon_h(2\delta - 2)}{\epsilon_h(2 + \delta) + \epsilon_{nc}(1 - \delta)}, \quad (1.7)$$

where ϵ_h and ϵ_{nc} are the bulk dielectric constants of the host matrix material and the NC material. For a matrix of organic ligands ($\epsilon_h = 2.2$) and PbS ($\epsilon_{nc,PbS} = 169$)⁶⁰ in a close packed configuration ($\delta = 0.74$), we obtain an upper limit of the dielectric constant of PbS NC-solids of $\epsilon_s = 18.5$, in good agreement with reported measurements.^{10,50,18,25}

If the NC-film is thin enough we can assume that the depletion region extends through the whole film, i.e. $W_D = d$. This approximation is helpful since W_D is often times unknown. This approximation can also be used to calculate the smallest possible value for the electrostatic capacitance:

$C_D > C_{D,0} = \epsilon_s \epsilon_0 / d$. For a typical 200 nm -thick PbS NC-solid, this lower bound on the electrostatic capacitance is between 62 nF/cm² and 82 nF/cm² assuming $\epsilon_s = 14 - 18.5$.^{18,25}

To understand what defines the width of the depletion region (W_D) we introduce the dielectric relaxation time of free charge carriers (τ_{rel}), which is given by

$$\tau_{rel} = \frac{\epsilon_s \epsilon_0}{\sigma} = \frac{\epsilon_s \epsilon_0}{e(\mu_n n + \mu_p p)}, \quad (1.8)$$

where σ is the conductivity and n and p are the density of free electrons and holes with respective mobilities μ_n and μ_p . When τ_{rel} exceeds the characteristic timescale of the measurement, which, for a harmonic capacitance measurement, is ω^{-1} , the charge carriers cannot follow and the material behaves like a electrostatic capacitor. As shown in Figure 6a, τ_{rel} varies over the semiconductor thickness depending on the local density of electrons and holes. The edge of the depletion region can now be defined as the point where $\tau_{rel}(x) = \omega^{-1}$.

In traditional semiconductor theory, it is often assumed that the mobility is high ($\mu_n \gg 10 \text{ cm}^2/\text{Vs}$) such that τ_{rel} in the bulk is in the range of ns to ps. These time scales are significantly shorter than the time scales of most capacitance measurement instrumentation (typically below 100 MHz). However, in low

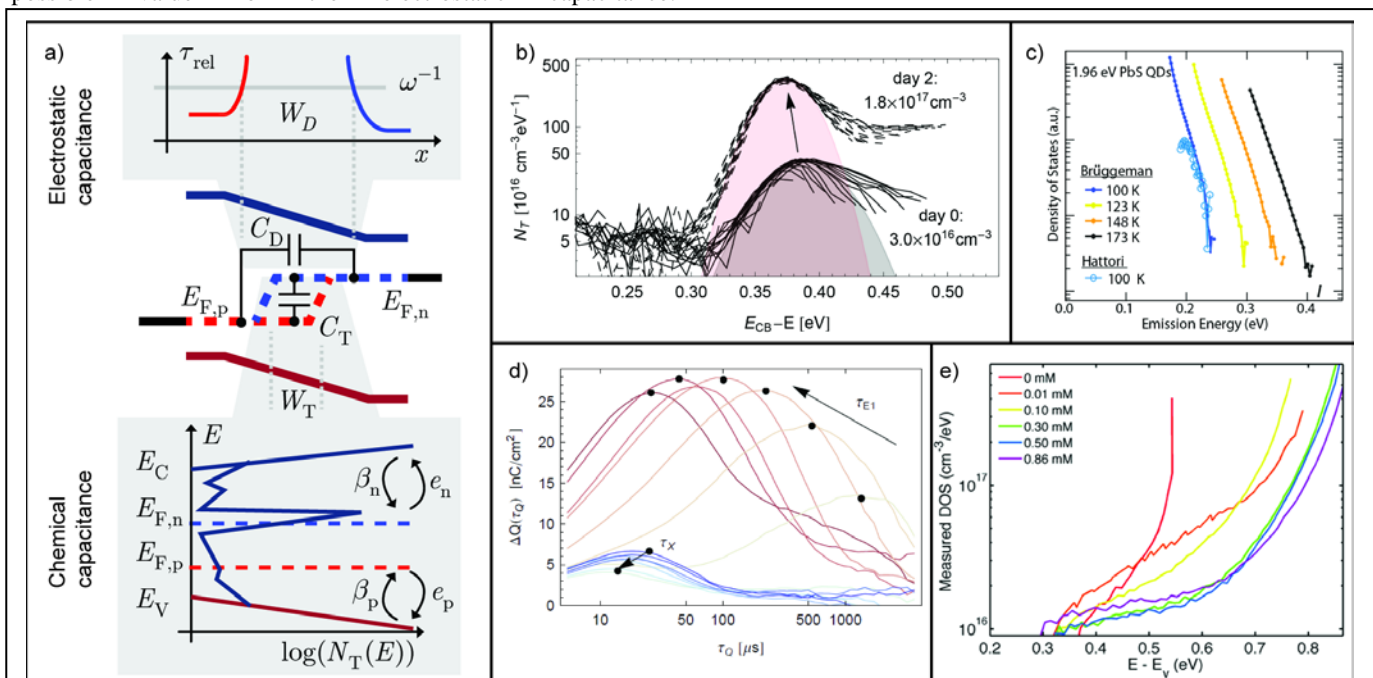


Figure 6: a) Schematic of the electrostatic (C_D) and chemical capacitance (C_T) in a diode. C_D is dominated by the width of the depletion region (W_D), which is defined by the divergence of the dielectric relaxation time (τ_{rel}). C_T is dominated by the density of states (N_T) and the position of the quasi-Fermi energies ($E_{F,n}$, $E_{F,p}$). The kinetics of the charge carriers contributing to C_T is given by the Shockley-Read-Hall capture (β_n, β_p) and emission (e_n, e_p) coefficients. b) N_T determined by thermal admittance spectroscopy (TAS) measurements.²⁵ c) N_T determined by IMPS measurements.⁴⁹ d) DLTS signal for different temperatures, indicating a discrete trap state with an activation-energy of 0.4 eV.⁵¹ e) N_T determined by transient open-circuit voltage (or differential capacitance) measurements.⁷⁶ Figures are reproduced from the indicated references.

mobility semiconductors such as PbS NC-solids, a typical relaxation time of $\tau_{\text{rel}} = 0.7 \mu\text{s}$ can be estimated assuming $\mu_p = 10^{-3} \text{ cm}^2/\text{Vs}$ and $p = 10^{16} \text{ cm}^{-3}$.⁵⁴ Thus τ_{rel} is in the range of most capacitance meters. Therefore to measure the depletion region, we cannot safely neglect the relaxation of free charge carriers and must carefully choose the measurement frequency. Further complicating the measurement of the depletion width is the second major contribution to the diode capacitance, the chemical capacitance.

The chemical capacitance,⁶¹ or equivalently the differential capacitance,^{62,30} is related to the occupation of electronic states in the semiconductor. The occupation of a discrete electron state "A" at an energy E_A in the Boltzmann approximation is:

$$n_A = N_A \exp\left(\frac{-(E_A - E_{F,n})}{kT}\right), \quad (1.9)$$

where $E_{F,n}$ is the quasi-Fermi energy of the electrons. If $E_{F,n}$ is changed, the occupation changes, requiring an addition or removal of electrons. This effect is conveniently described by the chemical capacitance⁶¹

$$C_{T,A} = e^2 \frac{\partial n_A}{\partial E_{F,n}} = e^2 \frac{n_A}{kT}, \quad (1.10)$$

which is a function of the $E_{F,n}$. Considering all electrons (n) in conduction band (CB) and trap states in a structure with a density of states $N_T(E)$, the chemical capacitance is given by

$$\begin{aligned} C_T &= e^2 \frac{\partial n}{\partial E_{F,n}} \\ &= e^2 \int N_T(E) f'(E - E_{F,n}) dE \approx e^2 N_T(E_{F,n}) \end{aligned} \quad (1.11)$$

where f' is the first derivative of the Fermi-Dirac distribution. The fact that the chemical capacitance is proportional to the density of states clarifies why capacitance can be used to characterize trap state density.

The absence of the dielectric constant in Eq. (1.12) highlights that the chemical capacitance is not of electrostatic origin and can therefore not be understood as a plate capacitor. Furthermore, the chemical capacitance has a unit of capacitance per volume (F/cm^3), so, to obtain the total chemical capacitance, Eq. (1.12) must be integrated along the film thickness. Assuming that the dominant contribution of the chemical capacitance comes from a region of width W_T , the total capacitance is given by:

$$C_T = e^2 N_T(E_{F,n}) W_T, \quad (1.12)$$

which has the unit of capacitance per area (F/cm^2). If we assume W_T is on the order of the film thickness, we find a typical value of $32 \text{ nF}/\text{cm}^2$ for a PbS NC-solid of thickness of 200 nm with a midgap state density of $10^{16} \text{ cm}^{-3} \text{ eV}^{-1}$.³⁰

The total capacitance of a diode is thus given by a combination of C_D and C_T where both capacitance contributions are comparable and on the order of $10 - 100 \text{ nF}/\text{cm}^2$. This

complicates the interpretation of measurement data, as most models are based on the assumption that only C_D or C_T is measured.

Qualitatively, we expect that the capacitance of a PbS NC-diode in the dark and open circuit condition, where only a low density of mobile charge carriers is available, will be dominated by the C_D . C_T will be comparatively low, reflecting the density of states in the middle of the band gap. Under increasing illumination or forward bias, more free charge carriers will be available. C_D will first increase and then disappear as τ_{rel} becomes faster than the timescale of the measurement. C_T will be significantly larger, as the quasi-Fermi energies for electrons and holes move towards the band edges, where the density of states increases.

Mott-Schottky Model

To interpret capacitance-voltage (CV) measurements, many authors apply the Mott-Schottky model.⁵⁶ In this model, it is assumed that the capacitance, C' , measured at a given frequency, ω , is dominated by the electrostatic capacitance of the depletion region and is given by:

$$C' \doteq C_D = \frac{\epsilon_s \epsilon_0}{W_D} = \sqrt{\frac{e \epsilon_s \epsilon_0 N_A}{2(V_{\text{bi}} - V)}}, \quad (1.13)$$

where N_A is the doping density and V_{bi} the built-in voltage. Eq. (1.14) can be used to determine N_A and V_{bi} by plotting C'^{-2} vs. V_D (Figure 3b). If a straight line can be fitted to this so-called Mott-Schottky plot, the x-axis intercept is taken as V_{bi} and the slope is related to N_A . Using this model, typical values for N_A are $1 - 5 \times 10^{16} \text{ cm}^{-3}$ and V_{bi} is around 0.55 V , corresponding to a depletion width at 0 V of $W_D = 200 - 250 \text{ nm}$.^{10,63,64,18}

Perhaps due to its seeming simplicity, the Mott-Schottky model is at times incorrectly applied to NC-based solids. For example, one common mistake found in literature is the use of the absolute value of the capacitance $|C| = \sqrt{C'^2 + C''^2}$ instead of the real part of the capacitance C' . In the forward region of a diode, large dc-currents pass through the diode and $|C|$ will approach C'' , since $C'' \propto \partial J_D / \partial V_D$. Plotting $|C|^{-2} = 1 / (C'^2 + C''^2)$ versus V_D leads to a plot with the typical Mott-Schottky shape, but the linear slope is simply a measure of the slope of the IV curve and cannot be used to extract N_A and V_{bi} .

Furthermore, it has not even been established that the Mott-Schottky analysis is applicable to NC-solids in general. To show this, it would be necessary to demonstrate that the measured capacitance is only weakly dependent on frequency and temperature in the region where the Mott-Schottky model is applied. If this is not the case, the capacitance is most probably dominated by the chemical capacitance of trap states instead of the electrostatic capacitance of the depletion region.

Unfortunately, confirming the validity of the Mott-Schottky analysis as applied in existing literature is difficult as very few articles report the raw capacitance spectrum prior to applying the inverse-square operation. In fact, the few studies, which report raw capacitance data, show anomalies, such as negative capacitances^{50,31} and increased bias dependence for thinner films³⁹, which are not consistent with the Mott-Schottky model. We note that raw capacitance spectra could provide additional insights into the physics of NC-solids. For example, the appearance of negative capacitances – which are reported but not commented upon in Refs. 50,31 – are in fact found in a large variety of electronic systems,⁶⁵ including metal-semiconductor interfaces,⁶⁶ Quantum-Well devices,⁶⁷ and general low-mobility semiconductors.^{68,69}

Shockley-Read-Hall Model

The trapping and detrapping of charge carriers plays a central role in the device operation of diodes and solar cells, in particular in materials with a high density of trap states, such as NC-solids. The kinetics of charge carrier trapping is usually described in the context of the Shockley-Read-Hall (SRH) model.^{56,70} In this model, the capture of electrons in a trap state located at an energy, E_T , below the conduction band is described by a capture coefficient (β_n) (See Figure 5a). The emission rate of an electron from the trap state to the conduction band at energy E_C is thus found to be:

$$e_n = \beta_n N_C \exp\left(\frac{-(E_C - E_T)}{kT}\right), \quad (1.14)$$

where N_C is the density of states of the conduction band. Coupling to the valence band follows the same formalism.

The pre-exponential factor in Eq. (1.15) is known as the attempt-to-escape frequency (or attempt-frequency) $\nu_0 = \beta_n N_C$.^{70,25} The temperature dependence of the ν_0 can be obtained within the effective mass approximation as

$$\nu_0 = \beta_n N_C = \nu_{00} T^2 = \sigma_T \Gamma_n T^2 \quad (1.15)$$

where ν_{00} is the reduced attempt frequency in units of $s^{-1}K^{-2}$, σ_T the trap capture cross section, and Γ_n a material dependent parameter for electrons given by:^{71,56}

$$\Gamma_n = 2 \times 3^{1/2} (2\pi / h^2)^{3/2} k^2 m_n^*, \quad (1.16)$$

where m_n^* is the effective mass of the electron. For bulk PbS, $\Gamma_n = 3.256 \times 10^{20} K^{-2} cm^{-2} s^{-1}$.⁵¹

Because the quadratic dependence of the attempt frequency on temperature is weak compared to its exponential dependence (Eq. (1.15)), this quadratic term is sometimes neglected.⁷⁰ We have therefore evaluated how both cases are related to each other: First we generate datasets for different values of E_T based on Eq. (1.15) where the pre-exponential factor of the emission rate is given by $\nu_{00} T^2$. We then fit these datasets with the same equation with a temperature-independent pre-exponential factor ν_0 . We find that by neglecting T^2

dependence, the activation energy is consistently overestimated by 39meV and that $\nu_0 = 4.0 \times 10^5 K^2 \nu_{00}$, for any given activation energy.

Trap State Characterization

Of particular interest in the optimization of NC-solids for solar cell performance is the reduction of trap states. Here, we summarize several approaches to quantify the energy and density of trap states in NC-solids from a variety of measurement data. These approaches invoke the models described above.

Thermal Admittance Spectroscopy

With the SRH model, it is possible to extract information about traps from the capacitance spectrum.⁷⁰ As shown in Figure 3a, a discrete trap state introduces a step in the capacitance spectrum at a frequency, which is given by the SRH model as

$$\omega_0 = 2\nu_0 \exp\left(-\frac{\Delta E_T}{kT}\right). \quad (1.17)$$

To determine the activation energy (ΔE_T) and the attempt-frequency (ν_0) of a trap state, the capacitance spectrum is recorded versus temperature. This is known as Thermal Admittance Spectroscopy (TAS). The trap state density in a diode can be reconstructed from the real part of the capacitance C' by:⁷⁰

$$N_T(E) = \frac{V_{bi}^2}{W_D (eV_{bi} - (E_{F,n,\infty} - E)) kT} \frac{1}{d\omega} \frac{\omega dC'(\omega)}{d\omega}, \quad (1.18)$$

where $E_{F,n,\infty}$ is the bulk Fermi-energy with respect to the conduction band as defined in Ref. 70. Using TAS, we have recently shown the presence of a discrete trap state in PbS:EDT NC-solids with a density of $1.8 \times 10^{17} cm^{-3}$ and an activation energy of $E_{T1} = 0.36eV$. The reduced attempt frequency for the T1 trap state was found to be $\nu_{00} = 1.2 \times 10^5 s^{-1}K^{-2}$, which corresponds to $\nu_0 = 4.8 \times 10^{10} s^{-1}$ according to the relation given above.²⁵

While TAS is a powerful and simple tool to detect trap states, trap states can be invisible to this technique.²⁵ A given trap state only contributes to the capacitance if the Fermi-energy crosses the trap level at some point in the device.⁷⁰ If this is not the case, the trap state will be invisible to TAS and can only be detected using complementary techniques.²⁵

Intensity-Modulated Photocurrent Spectroscopy

Also based on the SRH model, intensity-modulated photocurrent spectroscopy (IMPS) measurements can be used to determine the number density of trap states.^{72,49} The frequency dependent photocurrent (Eq. (1.3)) is used to reconstruct the trap state density:

$$N_T(E) \propto \frac{\partial \cos \varphi_{D,ph}(\omega)}{\partial \log \omega |J_{D,ph}(\omega)|}. \quad (1.19)$$

IMPS measurements on PbS:EDT NC-solids by Erslev *et al.* indicate that the band edge of the material has an exponential trap distribution of only 15meV, comparable with polycrystalline semiconductors and significantly lower than for amorphous silicon (See Figure 6c). Additionally, they identify a discrete trap state with an activation energy of $E_T = 0.25\text{eV}$ and an attempt frequency of $\nu_n = 5.0 \times 10^5\text{s}^{-1}$.

Deep Level Transient Spectroscopy

A more direct approach to detect the emission of trapped charge carriers (Eq. (1.15)) is deep level transient spectroscopy (DLTS), which is based on a large signal transient measurement.⁷³ In the original DLTS method, the diode is first excited by a voltage pulse, after which the transient of C' is recorded. C' is typically measured at 1 MHz using a capacitance bridge (e.g. Boonton 7200). This method is based on the assumptions that:

- 1) At the chosen measurement frequency, the chemical capacitance of the trap states is negligible in comparison to the electrostatic capacitance.
- 2) The dielectric relaxation time of free charge carriers $\tau_{rel} = \epsilon_s / \sigma$ is much shorter than the inverse measurement frequency (i.e. free charge carriers can move instantaneously at the chosen measurement frequency).

We recently showed that trap states contribute significantly to the capacitance of PbS NC-diodes up to a frequency of 20kHz at room temperature.²⁵ The dielectric relaxation time of free carriers in PbS NC-solids can be estimated to be on the order of $1\mu\text{s}$, restricting the measurement frequency to $\ll 160\text{kHz}$. Since the trap response frequency and the dielectric relaxation frequency differ by less than an order of magnitude, we conclude that transient capacitance measurements cannot be interpreted within the standard theory of DLTS. Previous capacitance based DLTS measurements on NC-diodes were therefore not conclusive.⁷⁴

An alternative DLTS method for high-trap density low-mobility semiconductors is given by Q-DLTS, which is based on the measurement of current transients. The current transient resulting from the carrier emission of a single discrete trap is given by:

$$J(t) = \frac{W_D N_T}{\tau_E} \exp\left(-\frac{t}{\tau_E}\right), \quad (1.20)$$

where the emission time constant is given by $\tau_E = e_n^{-1}$.

In the presence of multiple trap states or a distribution of trap states, the measured current transient ($J_D(t)$) will be the sum of the individual contributions and become multi-exponential. The measured current transients can be processed by the box-

car correlation method, parameterized by two times t_1 and t_2 , which are typically chosen with a fixed ratio $t_2 / t_1 = 2$. The DLTS signal (ΔQ) is then given by

$$\Delta Q(\tau_Q) = \int_{t_1}^{t_2} J_D(t) dt, \quad (1.21)$$

$$\tau_Q = \frac{t_2 - t_1}{\log t_2 / t_1},$$

where τ_Q is the detector time constant. Intuitively, one can think of $\Delta Q(\tau_Q)$ as an approximation of the distribution of time-constants present in the decay of $J_D(t)$.

A typical trace for $\Delta Q(\tau_Q)$ is shown in Figure 6d, where the large peak indicates a single emission time constant. The number of traps can be determined from the peak value (ΔQ_{max}):

$$N_T = \frac{4\Delta Q_{max}}{eW_D}. \quad (1.22)$$

We have applied Q-DLTS to PbS:EDT NC-diodes and have reported the measurement of a trap state with an activation energy of $\Delta E_T = 0.36\text{eV}$ and density of $\sim 2 \times 10^{17}\text{cm}^{-3}$ in agreement with TAS measurements.^{51,25}

Charge Extraction by Linearly Increasing Voltage (CELIV)

A second technique based on transient current measurements is known as charge extraction by linearly increasing voltage (CELIV).^{52,53} As shown in Figure 4a, a linear voltage ramp with speed $dV_D / dt = s$ is applied and the current is measured.⁵⁰ A flat plateau of the current is interpreted as the displacement current of the electrostatic capacitance and is used to estimate the dielectric constant

$$\epsilon_s \epsilon_0 = \frac{J_D W_D}{s}. \quad (1.23)$$

CELIV was applied to PbS NC-diodes to find $\epsilon_s = 17 \pm 2$ and $\epsilon_s = 18$, which is in line with effective medium theory.^{50,10} In the report by Johnston *et al.* CELIV is also used to determine the majority carrier (hole) mobility to $1.5 \times 10^{-3}\text{cm}^2\text{V}^{-1}\text{s}^{-1}$.⁵⁴

Transient open-circuit voltage

Transient open-circuit voltage measurements, also known as differential capacitance measurements, are another approach to determine the chemical capacitance of trap states. These techniques have been used extensively in the field of dye-sensitized solar cells,⁵⁵ organic solar cells,^{62,75} and have recently been applied to PbS NC-solids.^{30,76}

To carry out these measurements, the diode is biased by constant illumination intensity (I_{ph}) and a short laser pulse introduces a small perturbation. The open-circuit voltage is measured versus time $V_{oc}(t)$ as shown in Figure 4c. For

different I_{ph} this trace is measured and three parameters are extracted: the open circuit voltage baseline ($V_{\text{oc},0}$), the differential open circuit voltage increase (ΔV_{oc}), and the small signal recombination time (τ_{rec}).

In a second experiment, the differential charge Δq is measured, which is the charge that is transported by the laser pulse from the valence to the conduction band. The same laser pulse as in the transient open-circuit voltage measurement is used to excite the diode without background illumination (i.e. $I_{\text{ph}} = 0$). The short circuit current (Figure 4c) is measured vs. time $J_{\text{sc}}(t)$, and Δq is found by the integration of the peak in $J_{\text{sc}}(t)$.

The differential capacitance (C_{DC}) is then calculated using Δq and the obtained pairs of values ($\Delta V_{\text{oc}}, V_{\text{oc},0}$):

$$C_{\text{DC}}(V_{\text{oc},0}) = \frac{\Delta q}{\Delta V_{\text{oc}}}$$

It is typically assumed that the differential capacitance represents the chemical capacitance of the trap states and that one of the quasi-Fermi energies (e.g. $E_{\text{F},\text{p}}$) is fixed and independent of the illumination. In this case, the quasi-Fermi energy of the other charge carrier can be expressed in terms of the open-circuit voltage: $E_{\text{F},\text{n}} = V_{\text{oc},0} - E_{\text{F},\text{p}}$ and the density of states can now be obtained by using Eq. (1.13):

$$\frac{C_{\text{DC}}(V_{\text{oc},0})}{e^2 W_{\text{T}}} \doteq \frac{C_{\text{T}}(E_{\text{F},\text{n}})}{e^2 W_{\text{T}}} = N_{\text{T}}(E_{\text{F},\text{n}}) \quad (1.24)$$

This technique has been applied to PbS NC-diodes to measure the midgap trap density (Figure 6e).^{30,76} Organically passivated PbS NC films were found to have a broad exponential distribution of trap states on the order of $10^{16} - 10^{17} \text{ cm}^{-3} \text{ eV}^{-1}$, some of which could be passivated with a hybrid approach using thiol-based and halide ligands.^{30,76}

For materials with a high dielectric constant, such as PbS NC-solids, the differential capacitance can be strongly influenced by the electrostatic capacitance of the depletion region, which introduces a baseline given by $\epsilon_{\text{s}} / (eW_{\text{D}})^2$. If the electrostatic capacitance is not subtracted from the differential capacitance, it will add a significant baseline to the obtained trap state density (e.g. $7.7 \times 10^{16} \text{ cm}^{-3} \text{ eV}^{-1}$ for a 100 nm film PbS NC film) and present a lower detection limit for trap states.

In addition to measuring the midgap trap density, transient open-circuit measurements enable investigation of the recombination dynamics that limit the open circuit voltage and have been used to assess different passivation schemes for PbS-based heterojunction devices.^{77,78} However, a detailed analysis of the recombination dynamics and its relation to trap states has not yet been carried out for PbS NC-materials.⁶²

Conclusions

In summary, a number of standard electrical characterization techniques can be applied successfully to NC-solids. However, the applicability of different models to interpret the data must be verified. This is particularly challenging in NC-solids because distinct processes occur on comparable time scales with similar magnitudes.

For example, we show that NC-solids have both electrostatic and chemical (differential) capacitance of comparable magnitude. However, the Mott-Schottky model considers only the electrostatic capacitance while the SRH-based models take only the chemical capacitance into account. Thus, the regimes of the applicability of these models to NC-solids must be carefully considered.

To emphasise the importance of carefully selecting models of the device physics, we show for example that seemingly different current-voltage data in literature reports are in agreement, if the diode model used for thin-film photovoltaics is consistently applied.

Presentation of quasi-static, harmonic, or transient data prior to analysis can greatly assist the community in achieving a deeper understanding the strengths and limitations of existing models and permit the eventual development of more comprehensive models, specifically aimed at NC solids.

Acknowledgements

The authors acknowledge funding support from Nano-Tera. D.B. is supported by the Swiss National Science Foundation through a research grant and the National Centre Competence in Research Quantum Sciences and Technology.

Notes and references

^a Laboratory for Nanoelectronics, ETH Zurich, denizb@ethz.ch.

^b Laboratory for Nanoelectronics, ETH Zurich, vwood@ethz.ch.

1. D. V Talapin, J.-S. Lee, M. V Kovalenko, and E. V Shevchenko, *Chem. Rev.*, 2010, **110**, 389–458.
2. Y. Shirasaki, G. Supran, M. Bawendi, and V. Bulović, *Nat. Photonics*, 2012, **7**.
3. G. Konstantatos and E. H. Sargent, *Nat. Nanotechnol.*, 2010, **5**, 391–400.
4. A. J. Nozik, M. C. Beard, J. M. Luther, M. Law, R. J. Ellingson, and J. C. Johnson, *Chem. Rev.*, 2010, **110**, 6873–90.
5. R. R. Lunt, T. P. Osedach, P. R. Brown, J. a. Rowehl, and V. Bulović, *Adv. Mater.*, 2011, **23**, 5712–27.
6. I. J. Kramer and E. H. Sargent, *Chem. Rev.*, 2013, 130920103133002.

7. J. Y. Kim, O. Voznyy, D. Zhitomirsky, and E. H. Sargent, *Adv. Mater.*, 2013.
8. F. Remacle and R. D. Levine, *Chemphyschem*, 2001, **2**, 20–36.
9. P. Würfel, *Physics of Solar Cells*, Wiley-VCH Verlag GmbH, Weinheim, Germany, 2005.
10. J. P. Clifford, K. W. Johnston, L. Levina, and E. H. Sargent, *Appl. Phys. Lett.*, 2007, **91**, 253117.
11. J. M. Luther, M. Law, M. C. Beard, Q. Song, M. O. Reese, R. J. Ellingson, and A. J. Nozik, *Nano Lett.*, 2008, **8**, 3488–92.
12. G. I. Koleilat, L. Levina, H. Shukla, S. H. Myrskog, S. Hinds, A. G. Pattantyus-Abraham, and E. H. Sargent, *ACS Nano*, 2008, **2**, 833–40.
13. K. W. Johnston, A. G. Pattantyus-Abraham, J. P. Clifford, S. H. Myrskog, D. D. MacNeil, L. Levina, and E. H. Sargent, *Appl. Phys. Lett.*, 2008, **92**, 151115.
14. W. Ma, J. M. Luther, H. Zheng, Y. Wu, and A. P. Alivisatos, *Nano Lett.*, 2009, **9**, 1699–703.
15. R. Debnath, J. Tang, D. A. Barkhouse, X. Wang, A. G. Pattantyus-Abraham, L. Brzozowski, L. Levina, and E. H. Sargent, *J. Am. Chem. Soc.*, 2010, **132**, 5952–3.
16. W. Ma, S. L. Swisher, T. Ewers, J. Engel, V. E. Ferry, H. A. Atwater, and A. P. Alivisatos, *ACS Nano*, 2011, **5**, 8140–7.
17. J. Tang, X. Wang, L. Brzozowski, D. A. R. Barkhouse, R. Debnath, L. Levina, and E. H. Sargent, *Adv. Mater.*, 2010, **22**, 1398–402.
18. P. R. Brown, R. R. Lunt, N. Zhao, T. P. Osedach, D. D. Wanger, L.-Y. Chang, M. G. Bawendi, and V. Bulović, *Nano Lett.*, 2011, **11**, 2955–61.
19. J. Gao, C. L. Perkins, J. M. Luther, M. C. Hanna, H. Chen, O. E. Semonin, A. J. Nozik, R. J. Ellingson, and M. C. Beard, *Nano Lett.*, 2011, **11**, 3263–6.
20. E. J. D. Klem, C. W. Gregory, G. B. Cunningham, S. Hall, D. S. Temple, and J. S. Lewis, *Appl. Phys. Lett.*, 2012, **100**, 173109.
21. M. T. Greiner and Z.-H. Lu, *NPG Asia Mater.*, 2013, **5**, e55.
22. C. Piliago, L. Protesescu, S. Z. Bisri, M. V. Kovalenko, and M. A. Loi, *Energy Environ. Sci.*, 2013, **6**, 3054.
23. K. Szendrei, W. Gomulya, M. Yarema, W. Heiss, and M. A. Loi, *Appl. Phys. Lett.*, 2010, **97**, 203501.
24. W. Yoon, J. E. Boercker, M. P. Lumb, D. Placencia, E. E. Foos, and J. G. Tischler, *Sci. Rep.*, 2013, **3**, 2225.
25. D. Bozyigit, S. Volk, O. Yarema, and V. Wood, *Nano Lett.*, 2013, **13**, 5284–8.
26. A. G. Pattantyus-Abraham, I. J. Kramer, A. R. Barkhouse, X. Wang, G. Konstantatos, R. Debnath, L. Levina, I. Raabe, M. K. Nazeeruddin, M. Grätzel, and E. H. Sargent, *ACS Nano*, 2010, **4**, 3374–80.
27. H. Liu, J. Tang, I. J. Kramer, R. Debnath, G. I. Koleilat, X. Wang, A. Fisher, R. Li, L. Brzozowski, L. Levina, and E. H. Sargent, *Adv. Mater.*, 2011.
28. J. Gao, J. M. Luther, O. E. Semonin, R. J. Ellingson, A. J. Nozik, and M. C. Beard, *Nano Lett.*, 2011, **11**, 1002–8.
29. J. Tang, K. W. Kemp, S. Hoogland, K. S. Jeong, H. Liu, L. Levina, X. Wang, R. Debnath, D. Cha, K. W. Chou, A. F. Aram, J. B. Asbury, E. H. Sargent, M. Furukawa, A. Fischer, and A. Amassian, *Nat. Mater.*, 2011, **10**, 765–71.
30. A. H. Ip, S. M. Thon, S. Hoogland, O. Voznyy, D. Zhitomirsky, R. Debnath, L. Levina, L. R. Rollny, G. H. Carey, A. Fischer, K. W. Kemp, I. J. Kramer, Z. Ning, A. J. Labelle, K. W. Chou, A. Amassian, and E. H. Sargent, *Nat. Nanotechnol.*, 2012, **7**, 577–82.
31. D. A. R. Barkhouse, R. Debnath, I. J. Kramer, D. Zhitomirsky, A. G. Pattantyus-Abraham, L. Levina, L. Etgar, M. Grätzel, and E. H. Sargent, *Adv. Mater.*, 2011, **23**, 3134–8.
32. I. J. Kramer, D. Zhitomirsky, J. D. Bass, P. M. Rice, T. Topuria, L. Krupp, S. M. Thon, A. H. Ip, R. Debnath, H.-C. Kim, and E. H. Sargent, *Adv. Mater.*, 2012, **24**, 2315–9.
33. K. S. Leschkie, A. G. Jacobs, D. J. Norris, and E. S. Aydil, *Appl. Phys. Lett.*, 2009, **95**, 193103.
34. X. Lan, J. Bai, S. Masala, S. M. Thon, Y. Ren, I. J. Kramer, S. Hoogland, A. Simchi, G. I. Koleilat, D. Paz-Soldan, Z. Ning, A. J. Labelle, J. Y. Kim, G. Jabbour, and E. H. Sargent, *Adv. Mater.*, 2013, **25**, 1769–73.
35. J. Jean, S. Chang, P. R. Brown, J. J. Cheng, P. H. Rekemeyer, M. G. Bawendi, S. Grateček, and V. Bulović, *Adv. Mater.*, 2013, **25**, 2790–6.
36. S. Kim, J. K. Kim, J. Gao, J. H. Song, H. J. An, T.-S. You, T.-S. Lee, J.-R. Jeong, E.-S. Lee, J.-H. Jeong, M. C. Beard, and S. Jeong, *ACS Appl. Mater. Interfaces*, 2013, **5**, 3803–8.
37. J. Tang, H. Liu, D. Zhitomirsky, S. Hoogland, X. Wang, M. Furukawa, L. Levina, and E. H. Sargent, *Nano Lett.*, 2012, **12**, 4889–94.
38. Z. Ning, D. Zhitomirsky, V. Adinolfi, B. Sutherland, J. Xu, O. Voznyy, P. Maraghechi, X. Lan, S. Hoogland, Y. Ren, and E. H. Sargent, *Adv. Mater.*, 2013, **25**, 1719–23.
39. A. K. Rath, M. Bernechea, L. Martinez, and G. Konstantatos, *Adv. Mater.*, 2011, **23**, 3712–7.
40. A. K. Rath, M. Bernechea, L. Martinez, F. P. G. de Arquer, J. Osmond, and G. Konstantatos, *Nat. Photonics*, 2012, **6**, 529–534.
41. J. M. Luther, J. Gao, M. T. Lloyd, O. E. Semonin, M. C. Beard, and A. J. Nozik, *Adv. Mater.*, 2010, **22**, 3704–7.
42. P. Stallinga, *Electrical Characterization of Organic Electronic Materials and Devices*, John Wiley & Sons, Ltd, Chichester, UK, 2009.

43. D. Abou-Ras, T. Kirchartz, and U. Rau, Eds., *Advanced Characterization Techniques for Thin Film Solar Cells*, Wiley-VCH Verlag GmbH & Co. KGaA, Weinheim, Germany, 2011.
44. K. Szendrei, M. Speirs, W. Gomulya, D. Jarzab, M. Manca, O. V. Mikhnenko, M. Yarema, B. J. Kooi, W. Heiss, and M. A. Loi, *Adv. Funct. Mater.*, 2012, **22**, 1598–1605.
45. J. R. Macdonald, *Ann. Biomed. Eng.*, 1992, **20**, 289–305.
46. M. Vanecek and A. Poruba, *Appl. Phys. Lett.*, 2002, **80**, 719.
47. H. Oheda, *J. Appl. Phys.*, 1981, **52**, 6693.
48. R. Brüggemann, C. Main, J. Berkin, and S. Reynolds, *Philos. Mag. Part B*, 1990, **62**, 29–45.
49. P. T. Erslev, H.-Y. Chen, J. Gao, M. C. Beard, A. J. Frank, J. van de Lagemaat, J. C. Johnson, and J. M. Luther, *Phys. Rev. B*, 2012, **86**, 155313.
50. J. Tang, L. Brzozowski, D. A. R. Barkhouse, X. Wang, R. Debnath, R. Wolowicz, E. Palmiano, L. Levina, A. G. Pattantyus-Abraham, D. Jamakosmanovic, and E. H. Sargent, *ACS Nano*, 2010, **4**, 869–78.
51. D. Bozyigit, M. Jakob, O. Yarema, and V. Wood, *ACS Appl. Mater. Interfaces*, 2013, **5**, 2915–9.
52. G. Juska, K. Arlauskas, M. Viliunas, J. Kocka, G. Juška, M. Viliunas, and J. Kočka, *Phys. Rev. Lett.*, 2000, **84**, 4946–4949.
53. a. J. Mozer, N. S. Sariciftci, L. Lutsen, D. Vanderzande, R. Österbacka, M. Westerling, and G. Juška, *Appl. Phys. Lett.*, 2005, **86**, 112104.
54. K. W. Johnston, A. G. Pattantyus-Abraham, J. P. Clifford, S. H. Myrskog, S. Hoogland, H. Shukla, E. J. D. Klem, L. Levina, and E. H. Sargent, *Appl. Phys. Lett.*, 2008, **92**, 122111.
55. P. R. F. Barnes, K. Miettunen, X. Li, A. Y. Anderson, T. Bessho, M. Gratzel, and B. C. O'Regan, *Adv. Mater.*, 2013.
56. S. Sze and K. Ng, *Physics of semiconductor devices*, 2006.
57. D. Neamen, *Semiconductor physics and devices*, McGraw-Hill, 4th editio., 2011.
58. C. Hyun Kim, O. Yaghmazadeh, Y. Bonnassieux, and G. Horowitz, *J. Appl. Phys.*, 2011, **110**, 093722.
59. U. Rau and H. Schock, *Appl. Phys. A Mater. Sci. Process.*, 1999, **69**, 131–147.
60. O. Madelung, *Semiconductors: Data Handbook*, Springer Berlin Heidelberg, Berlin, Heidelberg, 2004.
61. J. Bisquert, *Phys. Chem. Chem. Phys.*, 2003, **5**, 5360.
62. C. G. Shuttle, B. O'Regan, A. M. Ballantyne, J. Nelson, D. D. C. Bradley, J. de Mello, and J. R. Durrant, *Appl. Phys. Lett.*, 2008, **92**, 093311.
63. G. I. Koleilat, X. Wang, A. J. Labelle, A. H. Ip, G. H. Carey, A. Fischer, L. Levina, L. Brzozowski, and E. H. Sargent, *Nano Lett.*, 2011.
64. Z. Ning, Y. Ren, S. Hoogland, O. Voznyy, L. Levina, P. Stadler, X. Lan, E. H. Sargent, and D. Zhitomirsky, *Adv. Mater.*, 2012, **24**, 6295–9.
65. A. K. Jonscher, *J. Mater. Sci.*, 1991, **26**, 1618–1626.
66. A. K. Jonscher, *J. Chem. Soc. Faraday Trans. 2*, 1986, **82**, 75.
67. M. Ershov, H. C. H. Liu, L. Li, M. Buchanan, Z. R. Wasilewski, and A. K. Jonscher, *IEEE Trans. Electron Devices*, 1998, **45**, 2196–2206.
68. H. Gommans, M. Kemerink, and R. Janssen, *Phys. Rev. B*, 2005, **72**, 235204.
69. E. Ehrenfreund, C. Lungenschmied, G. Dennler, H. Neugebauer, and N. S. Sariciftci, *Appl. Phys. Lett.*, 2007, **91**, 012112.
70. T. Walter, R. Herberholz, C. Muller, and H. W. Schock, *J. Appl. Phys.*, 1996, **80**, 4411.
71. O. Gaudin, R. B. Jackman, T.-P. Nguyen, and P. Le Rendu, *J. Appl. Phys.*, 2001, **90**, 4196.
72. K. Hattori, Y. Niwano, H. Okamoto, and Y. Hamakawa, *J. Non. Cryst. Solids*, 1991, **137-138**, 363–366.
73. D. V. Lang, *J. Appl. Phys.*, 1974, **45**, 3023.
74. R. Loef, A. J. Houtepen, E. Talgorn, J. Schoonman, and A. Goossens, *J. Phys. Chem. C*, 2009, **113**, 15992–15996.
75. B. C. O'Regan, S. Scully, A. C. Mayer, E. Palomares, and J. Durrant, *J. Phys. Chem. B*, 2005, **109**, 4616–23.
76. S. M. Thon, A. H. Ip, O. Voznyy, L. Levina, K. W. Kemp, G. H. Carey, S. Masala, and E. H. Sargent, *ACS Nano*, 2013.
77. N. Zhao, T. P. Osedach, L.-Y. Chang, S. M. Geyer, D. Wanger, M. T. Binda, A. C. Arango, M. G. Bawendi, and V. Bulovic, *ACS Nano*, 2010, **4**, 3743–52.
78. K. W. Kemp, A. J. Labelle, S. M. Thon, A. H. Ip, I. J. Kramer, S. Hoogland, and E. H. Sargent, *Adv. Energy Mater.*, 2013, **3**, 917–922.